ISSN 0252-1075
Research Report No. RR-072

Contributions from
Indian Institute of Tropical Meteorology

DEVELOPMENT OF SIMPLE REDUCED GRAVITY OCEAN MODEL FOR THE STUDY OF UPPER NORTH INDIAN OCEAN

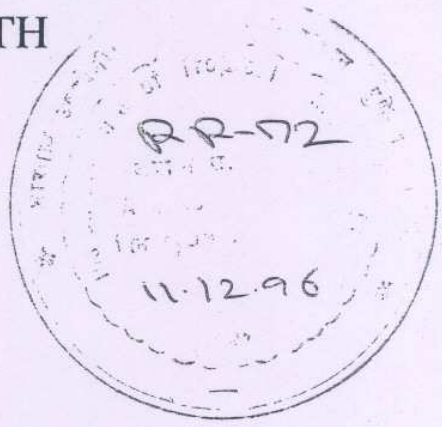

by

S.K.BEHERA
and
P.S.SALVEKAR

PUNE - 411 008
INDIA

NOVEMBER 1996

Contents

Development of simple reduced gravity ocean model for the study of upper North Indian Ocean.

S.K. Behera & P.S. Salvekar
Indian Institute of Tropical Meteorology, Pune-8, India

Abstract

A simple reduced gravity ocean model is formulated to simulate the upper layer circulation of north Indian Ocean. Complete numerical formulation of the model is presented. The model geometry includes the entire north Indian Ocean north of 25S. Radiation boundary condition is employed at open sea sides. Monthly mean wind stress derived from FSU pseudo-stress data for the period 1977-1986 is used to force the model. The model is able to produce most of the observed features of the seasonal upper layer circulation of the Indian Ocean with an initial depth of 200 meter and the ten years averaged mean monthly wind stress. However, some inconsistency is noticed in the simulated summer circulation in the Bay of Bengal. In order to overcome this model deficiency initial depth is reduced to 100 meter. This resulted in a slower initial baroclinic mode. The simulated circulation in the later case is found more realistic through out the year and over most part of the basin.

Many sensitivity experiments are carried out. Interannual variability in the wind forcing produces interannual variability in model circulation features near the Somali Coast, in the Bay of Bengal and east of Madagascar. Longitude time cross sections of upper layer thickness anomalies show, in general, eastward propagation in northern Indian Ocean during bad monsoon years which were happen to be ElNino years.

An attempt is made to include thermodynamics in the model. The simulated SSTs are quite close to the observed SST in the interior Arabian Sea and Bay of Bengal but not near coastal region and in the southern Indian Ocean.

1. Introduction

Land locked from three sides, and dynamically rich in response to the reversing monsoon winds, north Indian Ocean has been providing an excellent opportunity for ocean studies. The strong monsoon winds influence the ocean locally and these local changes in the upper ocean in turn excite propagating signals through ocean waves that travel large distances to influence other parts of the ocean, remotely. Extensive observational and modelling studies have been attempted relating to the problems of northwestern sector and the equatorial region of the Indian Ocean but relatively less effort0s have been made so far to understand the physical and dynamical processes of the Bay of Bengal and coastal region around India.

Following the work of Cox (1970), in the last two decades there have been considerable mathematical modelling work for the Indian Ocean, e.g. Luther et al. (1985), Luther & O' Brien (1989), McCreary & Kundu (1988), Das et al (1987), Jensen (1990). Cox (1970) used a three dimensional oceanic general circulation model with seven levels in vertical direction, where as most of the other workers used layer models with assumption of one or more active layers over an infinitely deep motionless layer. These layer models with less vertical resolution and less prognostic equations require relatively small computational resources compared to oceanic general circulation models. These models do not include prognostic thermohaline equations, but due to their computational efficiency they can be used for several numerical experiments to study their sensitivity to various forcings, boundary conditions and geometries. These models can also be modified to include additional physics, e.g. Zebiac and Cane (1987) added a mixed layer of constant depth with thermodynamics on the top of the upper layer and coupled the ocean model to a simple atmosphere model (Gill 1980) to study the ENSO phenomenon.

Luther et al. (1985) using two different wind forcing, simulated realistically the Somali Current and the associated gyre system, Luther & O' Brien (1989), using 23 year mean monthly wind data (Cadet and Diehl 1984) showed the interannual variability in Somali Current and the Indian Ocean. Jensen (1990) simulated the subsurface circulations besides the surface circulation of the Indian Ocean using a three and half layer model. Dube et al. (1990) investigated the relationship between the interannual variability in model fields and the Indian monsoon rainfall. In the present study, a simple one and half layer reduced gravity transport model is formulated and used to study the wind driven ocean circulation of the upper north Indian Ocean and also used to determine the interannual variability.

It seems that the coastal circulation plays an important role in the linking process between Arabian Sea and Bay of Bengal. Ship drift observations (Rao et al. 1991), satellite derived inferences (Legeckis 1987) and model results (Potemra et al. 1991 and McCreary et al. 1993, hereafter MKM) indicate a southward boundary current along east coast of India during winter months. The observed surface currents are northward along the west coast during that period (Shetye and Shenoi, 1988 hereafter SS). These coastal currents together with the North Equatorial Current south of Sri Lanka provide a basis for a linking mechanism between the two basins. The northward currents along west coast during northeast monsoon discard the direct forcing mechanism by the along shore winds. But reverse phenomena occurs during summer months and the currents from west coast (southward) to east coast (northward) complete the circulation.

Remote forcing mechanisms play an important role in determining the circulation features around the Indian coast. The model results of Potemra et al. 1991 and Yu et al. 1991 have shown that Rossby waves originated from coastal Kelvin waves from eastern rim of the Bay of Bengal, determine to a large extent the circulation features in Bay of Bengal and currents along east coast of India. The modelling study of MKM suggest the more dominating role of local wind forcing on the circulation along east coast of India and dominating influence of remote forcing from the Bay of Bengal on the west coast circulation all through the year by propagating coastal Kelvin waves.

2.Model Formulation

2.1 Basic Equations

The following basic governing equations for momentum and mass conservation in Cartesian coordinate are used to formulate the model equations. The x, y and z coordinates are positive eastward, northward and downward respectively. z=0 is the surface of the ocean at rest.

The two momentum equations are

$$\frac{du}{dt} - fv + \frac{1}{\rho}\frac{\partial p}{\partial x} = A_H \nabla^2 u + \frac{\partial}{\partial z}\left(A_v \frac{\partial u}{\partial z}\right) \tag{1}$$

$$\frac{dv}{dt} + fu + \frac{1}{\rho}\frac{\partial p}{\partial y} = A_H \nabla^2 v + \frac{\partial}{\partial z}\left(A_v \frac{\partial v}{\partial z}\right) \tag{2}$$

Here, the total derivative is defined as

$$\frac{d}{dt} = \frac{\partial}{\partial t} + \vec{\mathbf{v}} \cdot \nabla \tag{3}$$

$\vec{\mathbf{v}}$ is the horizontal velocity vector and u, v are the components of the vector, $f = 2\,\Omega \sin\varphi$ is the Coriolis parameter, A_H and A_v are the horizontal and vertical eddy viscosity coefficients. The vertical velocity is neglected in these two equations, assuming that the horizontal scale of motion is larger than the vertical.

Considering constant density in the layer i.e.

$$\frac{d\rho}{dt} = 0 \tag{4}$$

the mass conservation equation can be written as

$$\frac{\partial u}{\partial x} + \frac{\partial v}{\partial y} + \frac{\partial w}{\partial z} = 0 \tag{5}$$

2.2 Formulation of the Physical Model

The model ocean consists of several layers of uniform density as shown in Fig. 1 with vertically uniform horizontal velocity in each layer. It is also assumed that all the layers have a positive thickness everywhere over entire time period i.e. the first layers is not allowed to surface and other layers are not allowed to merge. However, a simpler 1.5 layer version of the model is actually used in this study as it represents the dominant mode of Indian Ocean.

In order to derive the model equation in transport form, the terms in the basic equations (1,2 & 5) are depth integrated in each layer. For example the zonal volume transport in a layer j is defined as

$$U_j = \int_{Z_{bj}}^{Z_{tj}} u_j dz = u_j H_j \tag{6}$$

where $H_j = Z_{tj} - Z_{bj}$ is the layer thickness.

Similarly meridional volume transport

$$V_j = v_j H_j \tag{7}$$

So, on vertically integrating the mass conservation equation (5) we get

$$\frac{\partial H_j}{\partial t} + \frac{\partial U_j}{\partial x} + \frac{\partial V_j}{\partial y} = 0 \tag{8}$$

similarly the two momentum equations (1 & 2) become

$$\frac{\partial U_j}{\partial t} + \frac{\partial}{\partial x}\left(\frac{U_j U_j}{H_j}\right) + \frac{\partial}{\partial y}\left(\frac{V_j U_j}{H_j}\right) - f V_j + \frac{H_j}{\rho_j}\frac{\partial p_j}{\partial x} = A_H \nabla^2 U_j + \left(\frac{\tau_j^{x,t}}{\rho_j} - \frac{\tau_j^{x,b}}{\rho_j}\right) \tag{9}$$

and

$$\frac{\partial V_j}{\partial t} + \frac{\partial}{\partial x}\left(\frac{U_j V_j}{H_j}\right) + \frac{\partial}{\partial y}\left(\frac{V_j V_j}{H_j}\right) + f U_j + \frac{H_j}{\rho_j}\frac{\partial p_j}{\partial y} = A_H \nabla^2 V_j + \left(\frac{\tau_j^{y,t}}{\rho_j} - \frac{\tau_j^{y,b}}{\rho_j}\right) \tag{10}$$

by considering $\rho A_v V = \tau$ *as the wind stress*. The superscript x and y stand for zonal and meridional components and t and b stand for top and bottom. The bottom stress is neglected in the model equations.

The pressure gradient term p is derived from hydrostatic relation, e.g. the hydrostatic pressure in the upper most layer in Fig 1 can be given by

$$p_1(Z) = p_a - g\rho_1 Z \tag{11}$$

where p_a is the atmospheric pressure (which can be neglected compared to oceanic pressure) and Z coordinate is negative in the ocean and zero at the surface $\eta(x,y)$. For deeper layers the layer top can be defined as

$$Z_{ij} = -\sum_{i=1}^{j-1} H_i \tag{12}$$

so that

$$p_j(Z) = p_{j-1}(Z_{ij}) - g\rho_j (Z - Z_{ij})$$

where the pressure at the top of layer j considered to be equal to the pressure at the bottom of layer j-1, hence,

$$p_{j-1}(Z_{ij}) = \sum_{i=1}^{j-1} g\rho_i H_i \tag{13}$$

neglecting the atmospheric pressure p_a. So the pressure gradient can be given as

$$\nabla p_j (Z) = \rho_j g \nabla\eta - \sum_{i=1}^{j-1} g(\rho_j - \rho_i) \nabla H_i \tag{14}$$

$$\textit{considering} \quad \nabla Z = -\nabla\eta = -\nabla \sum_{i=1}^{N} D + H_i \; ; \; D \textit{ is the total depth} \tag{15}$$

The pressure gradient term (14) can be integrated vertically by multiplying with H_j, the layer depth.

2.3 The Reduced Gravity Assumption :

Different numerical models have different methods to deal with the barotropic gravity wave of large phase speed, that limits the model time step. In this model, pressure gradient in the lowest layer is assumed to be vanishingly small, resulting in a motionless condition in the layer. This assumption removes the barotropic mode. So, from Eq. 14, we get (for j=N)

$$\nabla\eta = \sum_{i=1}^{N-1} \frac{\rho_N - \rho_i}{\rho_N} \nabla H_i \tag{16}$$

where N is the total number of layers in the model. For example N=4 and N=2 gives a 3.5 layer model and a 1.5 layer model respectively. The lower inactive layer is considered as half layer in these models. We only use the 1.5 layer model results in most of the discussions of the following sections. In the 1.5 layer model the pressure gradient term becomes

$$\frac{1}{\rho_1}\nabla p_1 = g' \nabla H_1 \; ; \quad \frac{H_1}{\rho_1}\nabla p_1 = g' H_1 \nabla H_1 = g' \nabla H_1^2 / 2$$
$$\textit{where } g' = \left(\frac{\rho_2 - \rho_1}{\rho_2}\right) g \tag{17}$$

is the reduced gravity. The modification in acceleration due to gravity in the model provides buoyancy to the layer. Since wind stress projects 20 times strongly on the first baroclinic mode as compared to the barotropic mode (Lighthill, 1969) the elimination of barotropic mode in the model is justified. Also the time scales of first baroclinic mode near equatorial region is much small (weeks) as compared to that of mid-latitudes (years).

2.4 Numerical Formulation

The model transport equations (8,9,10) are solved numerically using central differences both in space. The spatial grid is staggered (Arawaka C grid) as in Fig.2. For time integration of the model equations Euler scheme is used at first time step and Leapfrog scheme is used for subsequent time steps. Euler scheme is used every 49th time step to eliminate the computational mode arising due to time splitting.

The parameters U, V and H are defined at the grid points (X_K, Y_L) located at longitudes,

$$\begin{aligned} (X_K)_U &= 2(K-1)\,\Delta X + X_o \\ (X_K)_V &= (X_K)_V - \Delta X \\ (X_K)_H &= (X_K)_V \;;\; K = 1,2,\ldots KMAX \end{aligned} \tag{18}$$

and at latitudes

$$\begin{aligned} (Y_L)_U &= 2(L-1)\,\Delta Y + Y_o \\ (Y_L)_V &= (Y_L)_U - \Delta Y \\ (Y_L)_H &= (Y_L)_U \;;\; L = 1,2,\ldots LMAX \end{aligned} \tag{19}$$

The terms in the equation (8,9 & 10) can be written in discretised form as follows :

i) Local Term

$$\frac{\partial H}{\partial t} = HL = \frac{H^{n+1}_{K,L} - H^{m}_{K,L}}{\Delta t^{*}} \tag{20}$$

where m = n-1 and $\Delta t^{*} = 2\Delta t$ for leap-frog scheme and m=n and $\Delta t^{*} = \Delta t$ for Euler scheme, used at 1st step and at every 49th time step.

Similarly,

$$\begin{aligned} \frac{\partial U}{\partial t} &= UL = \frac{U^{n+1}_{K,L} - U^{m}_{K,L}}{\Delta t^{*}} \\ \frac{\partial V}{\partial t} &= VL = \frac{V^{n+1}_{K,L} - V^{m}_{K,L}}{\Delta t^{*}} \end{aligned} \tag{21}$$

ii) Divergence term

$$\frac{\partial U}{\partial x} + \frac{\partial V}{\partial y} = HDV = \frac{U_{K,L} - U_{K-1,L}}{2\Delta X} + \frac{V_{K,L+1} - V_{K,L}}{2\Delta Y} \tag{22}$$

iii) Advection term

$$\frac{\partial}{\partial x}\left(\frac{U^2}{H}\right) + \frac{\partial}{\partial y}\left(\frac{UV}{H}\right) = UAD = \frac{1}{2\Delta X}\left[\frac{(U_{K+1,L} + U_{K,L})^2}{4H_{K+1,L}} - \frac{(U_{K,L} + U_{K-1,L})^2}{4H_{K,L}}\right] + \frac{1}{2\Delta Y}\left[\frac{(U_{K,L+1} + U_{K,L})(V_{K,L+1} + V_{K+1,L+1})}{(H_{K,L} + H_{K+1,L} + H_{K+1,L+1} + H_{K,L+1})} - \frac{(U_{K,L} + U_{K,L-1})(V_{K,L} + V_{K+1,L})}{(H_{K,L-1} + H_{K+1,L-1} + H_{K+1,L} + H_{K,L})}\right] \tag{23}$$

and

$$\frac{\partial}{\partial x}\left(\frac{UV}{H}\right) + \frac{\partial}{\partial y}\left(\frac{V^2}{H}\right) = VAD = \frac{1}{2\Delta X}\left[\frac{(U_{K,L} + U_{K,L-1})(V_{K+1,L} + V_{K,L})}{(H_{K,L-1} + H_{K+1,L-1} + H_{K+1,L} + H_{K,L})} - \frac{(U_{K-1,L} + U_{K-1,L-1})(V_{K,L} + V_{K-1,L})}{(H_{K-1,L-1} + H_{K,L-1} + H_{K,L} + H_{K-1,L})}\right] + \frac{1}{2\Delta Y}\left[\frac{(V_{K,L+1} + V_{K,L})^2}{4H_{K,L}} - \frac{(V_{K,L} + V_{K,L-1})^2}{4H_{K,L-1}}\right] \tag{24}$$

iv) Coriolis term

$$fV = UCR = 2\Omega \sin\varphi_L \, (V_{K,L} + V_{K+1,L} + V_{K+1,L+1} + V_{K,L+1}) \, / \, 4$$

$$fU = VCR = 2\Omega \sin\varphi_{L-1/2} \, (U_{K-1,L-1} + U_{K,L-1} + U_{K,L} + U_{K-1,L}) \, / \, 4 \tag{25}$$

v) Pressure gradient term

$$\frac{H}{\rho}\frac{\partial p}{\partial x} = \frac{g'}{2}\frac{\partial H^2}{\partial x} = UPR = \frac{g'}{2}\left[\frac{(H_{K+1,L})^2 - (H_{K,L})^2}{2\Delta X}\right]$$

$$\frac{H}{\rho}\frac{\partial p}{\partial y} = \frac{g'}{2}\frac{\partial H^2}{\partial y} = VPR = \frac{g'}{2}\left[\frac{(H_{K,L})^2 - (H_{K,L-1})^2}{2\Delta Y}\right] \tag{26}$$

vi) Diffusion term

$$A_H \nabla^2 U = UDF = A_H \left[\frac{U_{K+1,L} + U_{K-1,L} - 2U_{K,L}}{4(\Delta X)^2} + \frac{U_{K,L+1} + U_{K,L-1} - 2U_{K,L}}{4(\Delta Y)^2} \right]$$

$$A_H \nabla^2 V = VDF = A_H \left[\frac{V_{K+1,L} + V_{K-1,L} - 2V_{K,L}}{4(\Delta X)^2} + \frac{V_{K,L+1} + V_{K,L-1} - 2V_{K,L}}{4(\Delta Y)^2} \right] \quad (27)$$

vii) Forcing term

$$\frac{\tau^x}{\rho} = UFR = \frac{\tau^x{}_{K,L}}{\rho}$$

$$\frac{\tau^y}{\rho} = VFR = \frac{\tau^y{}_{K,L}}{\rho} \quad (28)$$

Hence equations 8,9 and 10 can be written as the following, in view of the above discretisation;

$$H_{K,L}{}^{n+1} = H_{K,L}{}^{m} - \Delta t^* (HDV)^n$$

$$U_{K,L}{}^{n+1} = U_{K,L}{}^{m} - \Delta t^* [(UAD)^n - (UCR)^n + (UPR)^n - (UDF)^n - (UFR)^m] \quad (29)$$

$$V_{K,L}{}^{n+1} = V_{K,L}{}^{m} - \Delta t^* [(VAD)^n + (VCR)^n + (VPR)^n - (VDF)^n - (VFR)^m]$$

The laplacian friction terms are evaluated at n-1 time level as central differencing with respect to time is unconditionally unstable for that term.

2.5 Boundary and Initial Conditions

The model geometry considered in this study covers the Indian Ocean north of 24S (Fig.3). All along the land boundaries, no slip boundary condition is applied i.e. both the components of transport vanishes ($U=V=0$) and along the open sea side of the southern boundary and along some part of the eastern boundary Camerlengo and O'Brien (1980) open boundary condition is used. Sri Lanka and Socotra islands are only considered in model geometry. One sided differences for space differentials are considered for the immediate grid points near to boundaries, if not resolved by no slip boundary condition.

At the open boundaries along the southern and eastern boundaries, a Sommerfeld radiation condition is applied to U, V and H fields (say ϕ)

$$\frac{\partial \phi}{\partial t} + C_\phi \frac{\partial \phi}{\partial x} = 0 \quad (30)$$

where ϕ can be any of the grid variables and C_ϕ is a phase speed. Hence, the values at the boundaries can be given as

$$\begin{aligned} \phi_B^{n+1} &= \phi_B^n \quad , & C_\phi \le 0 \\ &= (1 - C_{\phi'})\phi_B^n + C_{\phi'}\phi_{B-1}^n, & C_\phi > 0 \end{aligned} \qquad (31)$$

$$\text{where} \quad C_{\phi'} = \min(C_\phi \frac{\Delta t^*}{\Delta x}, 1)$$

and C_ϕ is computed numerically from (30).

However, the boundary condition does not ensure a complete non-reflection along the open boundaries. Hence the model fields are smoothed at these boundary points using a Hanning filter, i.e

$$\phi_{K,L} = 0.25 * \phi_{K,L} + 0.13(\phi_{K-1,L} + \phi_{K+1,L} + \phi_{K,L+1}) + 0.05(\phi_{K-1,L-1} + \phi_{K+1,L-1} + \phi_{K-1,L+1} + \phi_{K+1,L+1})$$

The filter is applied to the two rows or columns of the model fields nearest to the open boundaries. For the boundary points a one sided smoothing is applied perpendicular to the boundary. The filter is applied at each 6th time step. Initial state of rest with a constant layer thickness of H_o = 200 m is considered as initial condition. The density difference between the active layer and the underlying inert lower layer is kept constant throughout the model integration. The parameter values used in the model are given in the following table.

Table 1: Parameters used in the model

Parameters	Symbol	Value
Reduced gravity	g'	0.03 m s^{-2}
Eddy viscosity coefficient	A_H	2250 m^2 s^{-1}
Grid length	ΔX and ΔY	28 Km
Time step	Δt	30 min
Density (air)	ρ_a	1.2 Kg m^{-3}
Density (water)	ρ_w	1026 Kg m^{-3}
Drag coefficient	C_D	$1.25*10^{-3}$

The present 1.5 layer version of the model requires about 1 hour CPU time in HP9000/735 workstation for one year of model integration. The model code is written in FORTRAN-77 and requires 300Kb of hard disk memory.

3. Results and Discussion

3.1 Model Input

The wind stress forcing used in the model is the 1 degree resolution monthly mean wind pseudo stress obtained from Florida State University which is based on COADS and NCDC data and objectively analyzed (Legler et al. 1989). Pseudo stress components are converted to stress components using a constant drag coefficient C_D and air density ρ_a for the period 1977-1986. Since in the present study the grid resolution is 28Km, a bicubic spline technique is then used to interpolate the data to get the input values at the model grid points. Figs. 4 and 5 show the 10 year averages of the considered period monthly mean wind stress and its curl respectively at bimonthly interval i.e starting from the month of January. The northeasterly wind dominate the model region north of equator during the months from November to March with the maximum wind stress in January. The more intense southwesterly wind dominate during the months from May through September and its maximum intensity is found during July-August. South of equator the wind stress is northward throughout the year with its maximum in July. The wind stress curl is negative over north-western sector of Arabian Sea in January. The extent of the negative curl increases spatially to cover whole basin in July. The maximum negative curl is also found during July. The negative curl over the basin is replaced by a positive curl in November. Most part of the Bay of Bengal is covered by the negative curl during January and the horizontal extent of the curl decreases in the succeeding months. A positive wind stress curl is seen over whole part of the basin in September. Throughout the year, negative curl is seen over most of the model region south of equator.

We assume that the monthly mean wind data represents the value at the middle of the respective month and then linearly interpolated between adjacent months to get the input at model time step. For simplicity model calendar is considered to be of 360 days and each month of 30 days.

3.2 Upper Layer Circulation

In the first experiment, the 10 year averages of the monthly mean wind stress for the considered period used as a forcing to spin up the model circulation from a state of rest. Initially the wind stress field is exponentially increased from zero to it's present value over 20 days (in order to avoid the excessive generation of internal waves) by multiplying the following factor;

$$\{ 1\text{-}EXP(t/t_0)\}$$

where t_0 =20 days and t is time. After approximately 7 to 9 years of model time integration, the model solutions reached a quasi-steady state. Therefore all the results from the tenth year of integration are discussed and are compared with the observational evidences and other model results. The current arrows in the figures are plotted from vector $\vec{v} = \vec{v}/|\vec{v}|^{1/2}$ which has the same direction of current $\vec{v}$ vector with an amplitude of $|\vec{v}|^{1/2}$. This modification enhances the weak flows compared to strong ones. The model fields shown in figures are the snapshots from middle of the respective months.

3.2.1 Somali Current and circulation in the Arabian Sea

The circulation features (Fig. 6) show the simulated annual upper layer current structure in the Indian Ocean. During Northern Hemisphere winter the winds are northeasterly in the north Indian Ocean and Somali Current along the Somali Coast flows southwestward. This is evident from the model January circulation (Fig. 6a). Model circulation fields show southward flow from December to early April. The flow is from 10N to equator in December and then flows up to 2S during Jan-Mar. The southward flowing Somali Current together with the northward flowing East African Coastal Current (EACC) form an anticyclonic gyre south of equator which is seen in January circulation (Fig. 6a). These model features are in qualitative agreement with the observed climatological atlases Duing (1970), Wyrtki (1971), Hasternath & Greischar (1989), Rao et al. (1991) and the model results of Luther & O' Brien (1989) and Woodbery et al. (1989).During the transition to southwest monsoon, the surface currents along the Somali Coast start flowing northward. Model results suggest a northward flow north of 5N fed by an onshore flow around 5N by late March (Fig. 6b) and northward all along the coast in April (not shown). This is in agreement with the climatological charts and as reported by Schott and Quadfasel (1982). The northward flow, north of 5N in March is reported to be in response to a local negative wind stress curl. However, the northward flow in model fields seems to be radiated from the west coast of India through the westward propagating downwelling Rossby waves (MKM). As the southward flowing Somali Current disappears in April and winds start blowing from southwest, the EACC reaches equator. The recirculated water from the EACC forms a cyclonic gyre south of equator in April. This becomes stronger in May (Fig. 6c) and is present through out the monsoon season. The offshore flow north of this gyre is just around equator against the observational evidence of 3N. Winds become stronger from May to August along the coast and coastal upwelling starts along the coasts in response to the nearshore positive wind stress curl which can be inferred from the model upper layer thickness (ULT) deviation (Fig. 7 c&d). The decrease of ULT is considered as an indicator of upwelling and vice versa.

An anticyclonic gyre which is known as Great Whirl forms around 5N in late July (Fig. 6d) and migrates northward in August. Another eddy called Socotra Eddy is found east of Socotra Island (55E,13N) in late July and August. These circulation features are in qualitative agreement with the earlier referred climatological atlases and as well as model studies. The formation and strengthening of the Great Whirl is often related with the negative wind stress curl which through Ekman pumping drives a similar circulation feature through geostrophic flow. The wind data used in the model shows negative wind stress curl to the east of the gyre (Fig. 5d). Observational evidences (Swallow & Fieux 1982) suggest a northward migration of the Southern Gyre and its subsequent merging with the Great Whirl in late August and early September which is also shown by the modelling study of Luther et al. (1985). In the present study northward migration of the Southern Gyre is not seen in model circulation but eddies from the gyre migrate northward and merged with Great Whirl. Luther & O' Brien (1989) suggested a blocking event north of Southern Gyre that prevented northward migration of the gyre in 7 of the 23 years of their model simulation. In this study there appears to be blocking event in both north and south of equator i.e. around 5N and 5S. The position and intensity of these eddies vary from year to year as these eddies arise in response to the signal in wind stress of the central equatorial region and propagated by Rossby waves.

In September the magnitude of southwesterly wind decreases but the circulation features are not far from the July features, except for the weakening of the Southern Gyre and northward migration of the Great Whirl (Fig. 6e). The ULT deviation fields suggest the westward propagation of upwelling Rossby wave from west coast of India (Fig. 7c,d&e). In November, the northeast monsoon arrives, but a northward coastal current (remnant of summer Somali Current) still found north of 7N (Fig. 6f) as indicated by observations. The anticyclonic eddies north of equator have disappeared, but the Southern Gyre is still present with an offshore flow around 2N. A basin wide cyclonic gyre is seen in the model circulation field over northwest Arabian Sea which is in agreement with observations. The gyre has developed in response to a low ULT field at the center of the basin that has been propagated from west coast of India.

The circulation in the interior Arabian Sea are mostly in Sverdrup balance throughout the year i.e. flowing southward in summer and northward in winter. The circulation features and the ULT deviation along the west coast of India are in contrast to what is expected from the wind field. The changes in ULT are more likely to be associated with the propagation of coastal Kelvin waves that are being generated by the wind perturbation near Sri Lanka.

3.2.2 South Equatorial Current (SEC)

Climatological charts suggest a broad westward flowing SEC between 8S and 20S in most part of the year. The model produced flows indicate a meandering westward current between 10S and 20S (Fig. 6). The climatological atlases also suggest a seasonal variability in SEC. In boreal summer it is broader and more to the north of its mean position whereas in corresponding winter it is narrow and to its south, which is found in the model circulation field (Fig. 6, i.e. the SEC east of 60E). This variability is generated by the annual cycle of the wind stress curl further east, which gives rise to westward propagating Rossby waves (Woodbery 1989).

The model SEC flows directly to the east coast of Madagascar as the model geometry does not include small islands east of Madagascar. It splits near Madagascar coast around 17S which is in agreement with observation (Schott et al. 1988). One branch of it flows south and goes out of model domain. The other branch flows around northern tip of Madagascar and again splits at African coast. One branch after splitting flows northward and feeds in to the EACC the other one flows southward as Mozambique Current. The basin wide southern hemisphere gyre is flanked by the SEC to south, the ECC to north , the EACC to west and the poleward flow from ECC to SEC at the lee of the minima of model ULT (Figs. 6 and 7) This is in response to the annual cycle in the wind field (the negative curl Fig. 5). The model produced ECC remains around equator between 3N and 7S and is affected by the westward propagating equatorial Rossby waves. The flow is eastward in most part of the year and together with the SEC forms the basin wide gyre in southern hemisphere. During transition months of the monsoon winds i.e Mar-Apr and Oct-Nov, model circulation shows a stronger ECC flowing around equator which is comparable to the observed Equatorial Jet (EJ). However observational evidences suggest a strong EJ covering whole of the equatorial belt during May and November (Wyrtki, 1973). The model produced EJ is seen earlier i.e. in March and October.

3.2.3 North Equatorial Current (NEC)

The model produced NEC changes direction four times in a year, flowing eastward during southwest monsoon. The eastward Monsoon Current(MC) generally observed in summer months is sometimes found to be shifted to north, being pushed northward by the westward propagating Rossby waves. This is mainly because the reported observed currents are wind driven surface currents where as the model currents are mean upper layer flow (from a depth of 200 m) governed by internal mode.

3.2.4 Circulation in Bay of Bengal

The model circulation for the Bay of Bengal can be broadly divided into four stages. In the first stage a large basin wide anticyclonic gyre (Fig. 6a) in winter months i.e. Dec-Mar dominates the circulation in the Bay which is in agreement with the climatological atlases and other model studies e.g. Potemra et al. (1991). The gyre has a northward flow along the east coast of India north of 13N in January as observed by Cutler and Swallow (1984) and inferred from satellite data by Legeckis (1987) and all along the east coast in subsequent four months (Fig. 6b&c). During the transition months i.e late March to early May the basin is devided by two gyres, a dominant anticyclonic gyre to the west and a weak cyclonic gyre to the east with northward flow along both the boundaries (Fig. 6b&c). The northward flow along the eastern rim of the bay is in response to the coastaly trapped Kelvin waves originated from reflected equatorial Kelvin waves at the eastern boundary. This wave in turn radiates downwelling westward Rossby wave that determines mostly the Bay circulation in subsequent months.

During late May and June the bay is dominated by a single cyclonic gyre which is replaced again by a weak two gyre system during Jul-Nov (Fig 6d,e&f). The flow during this stage is southward along both the boundaries (Fig. 6d,e&f), with a cyclonic gyre to west and an anticyclonic gyre to the east. The model produced southward flow during summer months along the east coast of India is not in agreement with the ship drift observations which suggest a northward flow during that period. The reason for such disagreement is mostly because the ship drift observed currents are from the upper few meters of the ocean where as the model currents are depth averaged flow of a layer which has an initial depth of 200m. The model behavior to a shallow initial depth of 100m is discussed in the next section.

3.3 Shallow initial depth case (H_0=100 m)

The model simulated circulation features discussed in the previous section show general disagreement with observational evidences in some part of the model region and during some period of the year. The model simulated EJ appears earlier than that suggested by observations. Great Whirl has a lesser spatial extent and is less intense. The southward flowing East Indian Coastal Current (EICC) during summer months are opposite to that suggested by ship drift observations. Most of the above discussed model deficiencies may be attributed to the fact that observational evidences compared in this study are mostly restricted to the upper few meters of the ocean where as the model produced circulation fields are depth averaged of the model upper layer which has an initial depth of 200 meter. In order to simulate such near surface features as discussed above, a 100 meter initial model layer thickness

is considered in this case. This change of model parameter will give rise to a slower initial internal mode i.e $(g'H)^{1/2}$ = 1.73 ms^{-1} as compared to a faster initial mode of 2.45 ms^{-1} in the previous case. The model simulated annual cycle of circulation and ULT deviations from the changed initial depth model simulation are shown in Figs. 8 & 9 respectively.

The strong EJ covering the whole equatorial belt is found in May and November in this case and is in good agreement with observations. The Great Whirl is clearly seen in this case (Fig. 8d) with a horizontal extent comparable to that suggested by observations. Also, the Southern Gyre found to move northward in this case in September. The EICC flows southward, south of 18N in January (Fig. 8a) in agreement with the ship drift observations. However, the July current chart (Fig. 8d) does not show a prominent northward flow as suggested by observations but current charts of June and August (not shown) suggest a northward flowing EICC. The SEC in this case found south of 15S throughout the year which is not in agreement with climatological atlases. This suggest the circulation over that region is dominated by a faster internal mode like the one discussed in the previous section. In general the model features with shallow initial depth show a greater degree of agreement with observations in the north Indian Ocean.

The variation in the model circulation in the two above discussed model simulations is obviously because of the chosen internal modes. Most of the agreement of the model circulation in the later case with that of the observations seems to be due to the slower propagation of Rossby waves in Arabian Sea and the Bay Bengal. Also a shallower layer is more prone to the Ekman forcing than a deeper layer. Hence, consideration of a shallower upper layer in such reduced gravity models will be more appropriate for simulation of the upper layer features of the north Indian Ocean.

3.4 Circulation around Indian Coasts

Since the model simulations from 100 meter initial depth case are closer to observations, the discussion in this section will be based on the results from the 100 meter case. The currents along west coast of India are mostly northward from November to March (Fig. 8) flowing into the weak northeasterly winds (Fig. 4). This indicates the less dominating role of direct wind forcing on the coastal circulation during this period. From April to October, the currents along west coast are mostly southward (Fig. 8). Since the local winds are generally southeastward (Fig. 4) and stronger than previous months, the local wind may be playing a dominant role in determining the circulation. Along east coast of India , the currents are generally southward from September to January (Fig. 8). The local winds are southwesterlies in September and October which become northeasterlies from November. This suggest a less important role of local wind on the initial development of the southward currents. Northward currents are generally found in model fields from February to August (a brief southward flow is also seen in July). Since the local winds become northward and stronger only from May, the initial establishment of the northward currents may not be because of the local winds.

3.5 Interannual Variability

In the second experiment, the model was integrated for an extended period of 10 years i.e from 11th to 20th year with the same wind as used in the first experiment, to study the

interannual variability in the model fields. From these last 10 years, we computed the mean and standard deviation(SD) of the model ULT field for the 16th of each month of the year at each grid point, e.g. 16th January of all the years and so on. The SD fields expressed as percentage of deviation from the mean are thus a indicator of the inherent interannual variability produced by the model physics and dynamics(since the wind cycle is the same repeating from year to year). The standard deviation of ULT fields are found to be less than 0.6% of the mean depth (1 m appx.) all over the basin.

When the same experiment was carried out with real time interannual winds (1977-86) the model fields show larger variability. The SD of the induced wind velocity magnitude for January and July months (Fig. 10a,b) shows higher variability in the equatorial Indian Ocean which is probably because of smaller wind magnitude and larger interannual variability. The SD of model ULT field for January 16th and July 16th as depicted in fig. 10(c,d) show everywhere at least an order of magnitude larger than the previous case, indicating that the variability in the model field is solely due to the variability in wind field. The higher variability in the model ULT field is near Madagascar and Somali Coast which indicates that the variability present in the model fields are not directly forced by local winds. It seems that the variability in the model fields near Madagascar Coast is because of the trapped energy from the blocking of the westward propagating Rossby waves which in turn might have been excited by the wind variability in the region farther east of Madagascar. Variability in model fields near Somali Coast seems also not to be directly forced by the prevailing local winds and are brought on from other regions by the seasonal currents. Highest and lowest variabilities are found in the months of October and May respectively. However, the months of January and July are chosen for discussion as representative months of winter and summer seasons.

The longitude-time cross section of ULT anomalies from 10 year average ULT are shown in figures 11, 12 & 13. The average anomaly in a 5 degree band between 7N and 12N shows general westward propagation of positive and negative phases of the anomalies in both Arabian Sea and Bay of Bengal (Fig. 11). However, in years 1981-82 and 1985-86, the anomalies also show an eastward propagation. These years are happen to be bad monsoon years in terms of the summer monsoon rainfall over India and also are ElNino years. In the other bad monsoon year of 1979 which was not an ElNino year, model ULT anomalies do not show eastward propagation. In the southern hemisphere in the corresponding latitude bands of 7S-12S, the anomalies are found to be stronger (Fig. 12). The anomalies generally show westward propagation and like northern hemisphere eastward propagation is found in 1985-86 but eastward propagation is not found in 1981-82. The phase of the annual cycle is relatively stationary in both the western and eastern section of the equatorial band (Fig. 13). In the central equatorial ocean again the signals are found to be propagating westward. However, eastward propagation of the anomalies are found in 1979, 1981-82 and 1985-86. The model ULT anomalies for the month of April i.e., one month prior to the onset of Indian summer monsoon in all the ten years are shown in fig 14. The positive anomaly is considered to be representative of warm anomaly and vice-versa. The model produced anomalies do not show any specific correspondence with the performance of Indian summer monsoon. The strong negative anomalies in the southern Indian Ocean in 1979 may be considered as a signal for a bad monsoon year. However, in other bad monsoon year like 1982 and 1985, the model ULT anomalies do not show similar features as seen in 1979. On the contrary the highest negative anomalies are seen in 1984 which was not a bad monsoon year.

4.Inclusion of Thermodynamics

The reduced gravity transport model described in section 3 is modified to include a temperature equation. It is assumed that the velocity fields and the height field affect the model upper layer temperature. However, the reverse interaction i.e. temperature affecting the other model variables is not considered. The model upper layer thickness is considered as the depth of mixed layer and the temperature thus produced is assumed to be a representative of SST. For the experiment in this section, the initial upper layer thickness is considered as $H_0 = 100$ m.

4.1 Temperature Diffusion Equation

The considered temperature diffusion equation is

$$\frac{\partial T}{\partial t} + u\frac{\partial T}{\partial x} + v\frac{\partial T}{\partial y} = K_T \nabla^2 T + \frac{1}{H}\left(\frac{Q}{\rho C_p} - W_e\ \Delta T\right) + (T_o - T)/t_r \qquad (33)$$

where T is the upper layer temperature, (u,v) are the velocity components, K_T is the thermal diffusion coefficient, H is the model upper layer thickness, Q is the net solar radiative flux at the surface of the model ocean, C_p is the specific heat capacity at constant pressure, W_e is the entrainment velocity. T_0 is the initial model upper layer temperature and t_r is the adjustment time. The last term is an artificial heating term is kept to avoid considerable cooling in the model temperature field in strong wind stress forcing regions like near Somali Coast.

The entrainment W_e is parameterised as

$$W_e = \begin{cases} \dfrac{P}{h(1 - m_e R_i^{-1})\Delta T} & P < 0 \\ 0 & P \geq 0 \end{cases} \qquad (34)$$

$$\text{where} \quad P = \frac{2mu_*^3}{\alpha g} - H\frac{Q}{\rho C_p}$$

is the net production of turbulent kinetic energy and m is the efficiency of generation. A constant value of ΔT = 4°C is considered in the entrainment term, the Richardson number is given as $R_i = \alpha g . \Delta T / |\Delta u|^2$, m_e is the efficiency of vertical current shear and u_* is the air frictional velocity which is proportional to wind speed i.e. $u_* = (\tau/\rho)^{1/2}$.

Since , in this study we have only considered a one active layer model, the vertical shear in the currents which is maximum near equatorial region is parameterised as,

$$\frac{m_e}{R_i} H = \frac{m_e}{\alpha g \Delta T} \Delta U^2 = h_e \mathrm{Exp}\left[-\frac{1}{2}\left(\frac{Y}{R}\right)^2\right] \qquad (35)$$

where h_e = 18 m is the maximum depth of upwelling, Y is meridional distance from equtor in kilometer and R = 300 km is the decay distance.

The temperature difference between upper active layer and lower inert layer is difficult to prescribe in a 1.5 layer model and hence parameterised in a simpler way as in MKM.

$$\Delta T = \begin{cases} T - T_e^{(y)} & T > T_e^{(y)} \\ 0 & T \le T_e^{(y)} \end{cases} \qquad (36)$$

where $T_e(y)$ is computed from the climatic SST values of the model region;

$$T_e^{(y)} = \left[\frac{1}{x_2 - x_1} \int_{x_1}^{x_2} clim\text{-}SST \right] - 2^{o}C \qquad (37)$$

so that this term ensures that the model SST will not cool beyond $T_e(y)$. The other parameter values are $K_T = 2250\ m^2\ s^{-1}$, t_r = 720 days , m = 1 and $\alpha = 2 \times 10^{-4}\ k^{-1}$

4.2 Discussion on SST simulation

The temperature equation like the other model equations are solved numerically keeping temperature values at the H grid points. The model equations are again time integrated for 9 years and the simulated SST fields from 10th year of integration are discussed. The same 10 year averaged (1977-86) monthly mean wind stress and surface net heat flux derived from COADS data are used as forcing in this experiment.

In January, the model simulated SST is relatively higher than the observed SST in extreme northern part of Arabian Sea and Bay of Bengal. In other region, the simulated SST is more closer to the observed SST. In July, the model simulated SST fields are more closer to observation in Arabian Sea and Bay of Bengal but are higher in eastern equatorial Indian Ocean and southern Indian Ocean. The model deficiency in producing realistic SST over some region is obviously due to the strong influence of wind in the parametrisation of vertical velocity component in the temperature equation. The parametrisation is being improved to produce more realistic SST.

5. Conclusion

The simple wind driven ocean circulation with only one active layer has simulated realistically most of the observed general circulation features of the Indian Ocean when forced with a repeating seasonal cycle of wind. The formation of Somali Currents and the associated gyres over time and space were realistic. The four stages in the circulation pattern of the Bay of Bengal as reported in the litrature was obtained by more sophisticated models, whereas the same realistic results are produced in this study with simpler 1.5 layer reduced gravity model. By reduction of initial model upper layer depth from 200 meter to 100 meter, the simulated circulation fields in the north Indian Ocean are found to be more realistic. The summer circulation of the Bay of Bengal is dominantly influenced by the response to the remote forcing from equatorial Indian Ocean through the downwelling Rossby waves originated from the coastally trapped Kelvin waves, propagating along the eastern boundary. The less agreement between observed currents and the model simulated currents along the east coast of India during mid summer months is due to the obvious differences between the shallow near surface real time currents and the model depth averaged currents from a relatively deeper layer. Longitude-time cross section of ULT anomalies show in general west ward propagation. However in bad monsoon years which are happen to be ElNino years, the ULT anomalies in the northern hemisphere show eastward propagation. The model produced ULT anomalies in the month of April i.e. one month prior to the monsoon onset over India, do not show any specific relationship with the performance of monsoon rainfall.

Acknowledgement : We are thankful to Director, IITM for continuous encouragement and support for the development of the model. We are grateful to Prof. J.J. O'Brien and Dr. J.N. Stricherz (Florida State University) for graciously supplying the wind data. We are also thankful to Dr. J.P. .McCreary (NOVA University, Florida) and Dr. M. Luther (University of Southern Florida) for providing useful comments and discussion on model results. Thanks are due to Mrs. A.A. Deo, Mr. D.W. Ganer and Mrs. S.S. Naik for their help during the preparation of the manuscript.

References :

Cadet, D.L. and Diehl, B.C. 1984, Interannual variability of surface fields over the Indian Ocean in recent decades, Mon. Wea. Rev., 112, 1921-1985.

Camerlengo, A.L. and O' Brien, J.J. 1980, Open boundary conditions in rotating fluid, J. Comp. Phys., 35, 12-35.

Cox, M.D. 1970, A mathematical model of the Indian Ocean, Deep Sea Res. 17, 47-75.

Cutler A.N. and Swallow, J.C. 1984, Surface currents in the Indian Ocean; compiled from historical data archived by the Meteorological Office, Bracknell, UK, Rep 187, 8pp

Das, P.K., Dube, S.K. and Rao, G.S., 1987, A steady state model of the Somali Current, Proc. Ind. Ac. Sci. 96, 279-290.

Dube, S.K., Luther, M.E. and O' Brien, J.J. 1990, Relationships between interannual variability in the Arabian Sea and Indian monsoon rainfall, Meteo. Atm. Phys., 44, 153-165.

Duing, W. 1970, The monsoon regime of the currents in the Indian Ocean, East-West Center Press, Honolulu, 68pp

Gill, A. E., 1980, Some simple solutions for heat induced tropical circulations, Q. Jr. of Roy. Met. Soc. 106, 447-462.

Hasternath, S. and Greischar, L.L. 1989, Climate atlas of the Indian Ocean, Part-III, Upper ocean structure, The University Of Wisconsin Press, 247 charts.

Jensen, T.G. 1990, A numerical study of the seasonal variability of the Somali Current, Ph. D. dissertation, Florida State Univ. 118pp.

Legeckis, R, 1987, Satellite observations of a western boundary current in the Bay of Bengal. J. Geophys. Res., 92, 12,974-12,978.

Legler, D.M., Navon, J.M. and O' Brien, J.J., 1989, Objective analysis of pseudostress over the Indian Ocean using a direct minimisation approach, Mon. Wea. Rev., 117, 709-720.

Lighthill, M.J.,1969, Dynamic response fo the Indian Ocean to onset of the southwest monsoon, Phil. Trans. Roy. Soci, A 265, 45-92.

Luther, M.E., O' Brien, J.J. and Meng, A.H. 1985, Morphology of the Somali Current system during the southwest monsoon; Coupled ocean-atmosphere models, Ed J.C.J. Nihoul, Elsevier Science Publ.

Luther, M.E. and O' Brien, J.J. 1989, Modelling the variability in Somali Current, Meso scale/Synoptic coherent structure in Geophysical turbulence; Eds J.C.J. Nihoul and B.M. Jamart, Elsevier Science Publ. 373-386.

McCreary, P.J. and Kundu, P.K. 1988, A numerical investigation of the Somali Current during the Southwest Monsoon, J. Mar. Res., 46, 25-58.

McCreary, P.J., Kundu, P.K., and Molinari, R.L., 1993, A numerical investigation of dynamics, thermodynamics and mixed layer processes in the Indian Ocean, Prog. Oceno. 31, 181-244.

Potemra, J.J., Luther, M.E. and O' Brien, J.J. 1991, Relationships between interannual variability in the Arabian Sea and Indian monsoon rainfall, J. Geophys. Res. 96,12,667-12,683.

Rao, R.R., Molinari, R.L., Festa, J.F. 1991, Surface meteorological and near surface oceanographic atlas of the tropical Indian Ocean, NOAA Technical Memorandum, ERL AOML-69.

Schott, F., Fieux, M., Kindle, J., Swallow, J. and Zantopp, R. 1988 The boundary currents east and north of Madagascar, Direct measurments and model comparison, J. Geophys. Res., 93, 4963-4974.

Schott, F. & Quadfasel D.R. 1982, Variability of the Somali current system during the onset of the southwest monsoon. J. Phys. Ocn. 12, 1343-1357.

Swallow, J.C. and Fieux, M. 1982, Historical evidence for two gyres in the Somali Current, J. Mar. Res., 40, 747-75 5.

Shetye S. R. & Shenoi SSC 1988, The seasonal cycle of surface circulation in the coastal north Indian Ocean, Proceeding of the Indian Academy of Sciences 93 (4) 399-411.

Woodberry, K.E., Luther, M.E. and O' Brien, J.J. 1989, The wind driven seasonal circulation in the southern tropical Indian Ocean, J. Geophys. Res., 94, 17,985-18,002.

Wyrtki, K. 1971, Oceanographic atlas of the International Indian Ocean Expedition, National Science Foundation, Washington, D.C. 531pp.

Wyrtki, K. 1973, An equatorial jet in the Indian Ocean, Science, 181, 262-264.

Yu, L., O'Brien, J. J. & Yang, J. 1991, On the remote forcing of the circulation in the Bay of Bengal, J. Geophys. Res, 96, 20, 449-20,454.

Zebiac, S.E. and Cane, M.A. 1987, A model ENSO, Mon. Wea. Rev. 115, 2262-2278.

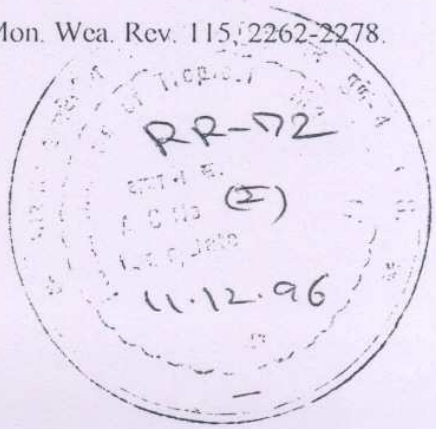

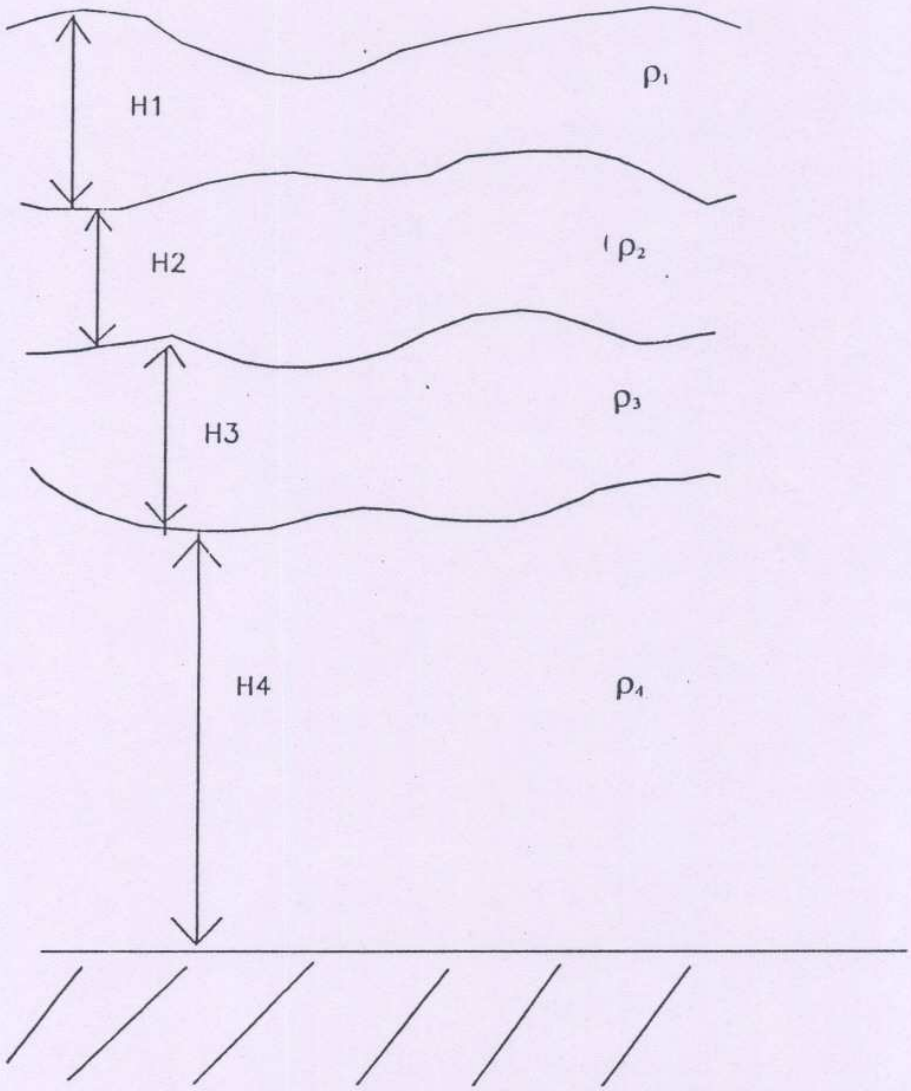

Fig. 1 : Schematic diagram of a four layer isopycnal model.

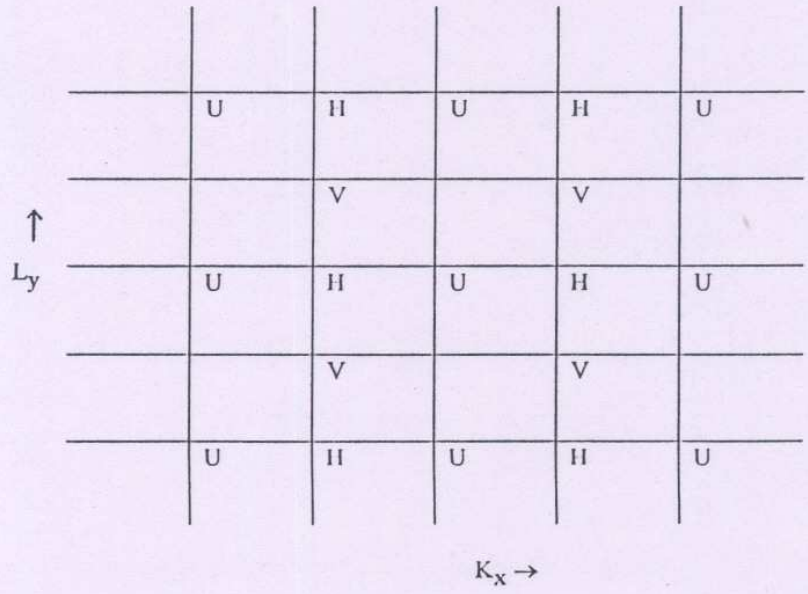

Fig. 2 : Distribution of model grid points (Arakawa – c)

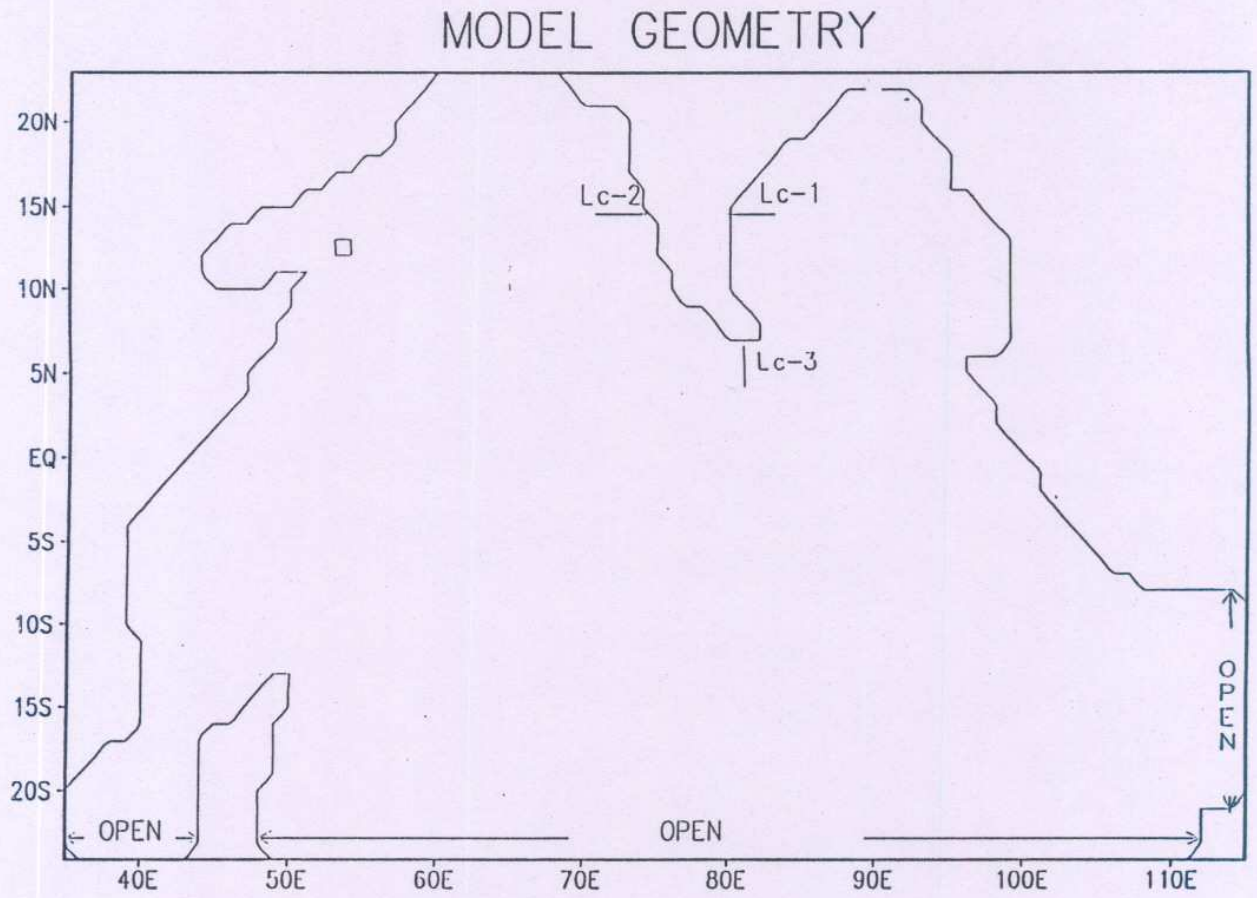

Fig. 3 : The model geometry, considered for numerical computation. Note the open boundaries to the south and in the east. Meridional transports are computed at section LC-1 & LC-2 and zonal transport is computed at LC-3.

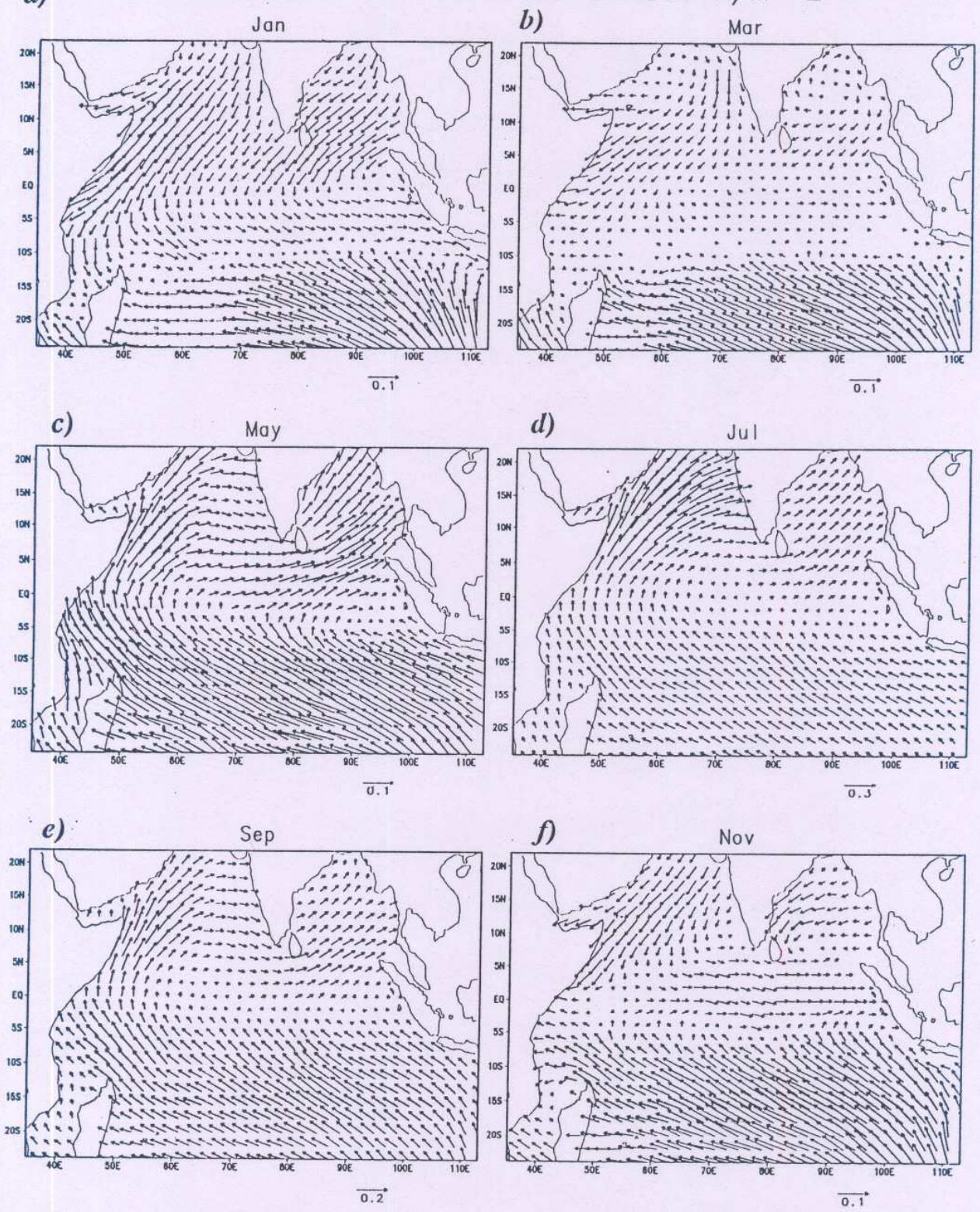

Fig. 4 : The ten year average (1977-86) FSU monthly mean wind stress over Indian Ocean in Nm^{-2} ; (a) January, (b) March, (c) May, (d) July, (e) September, and (f) November.

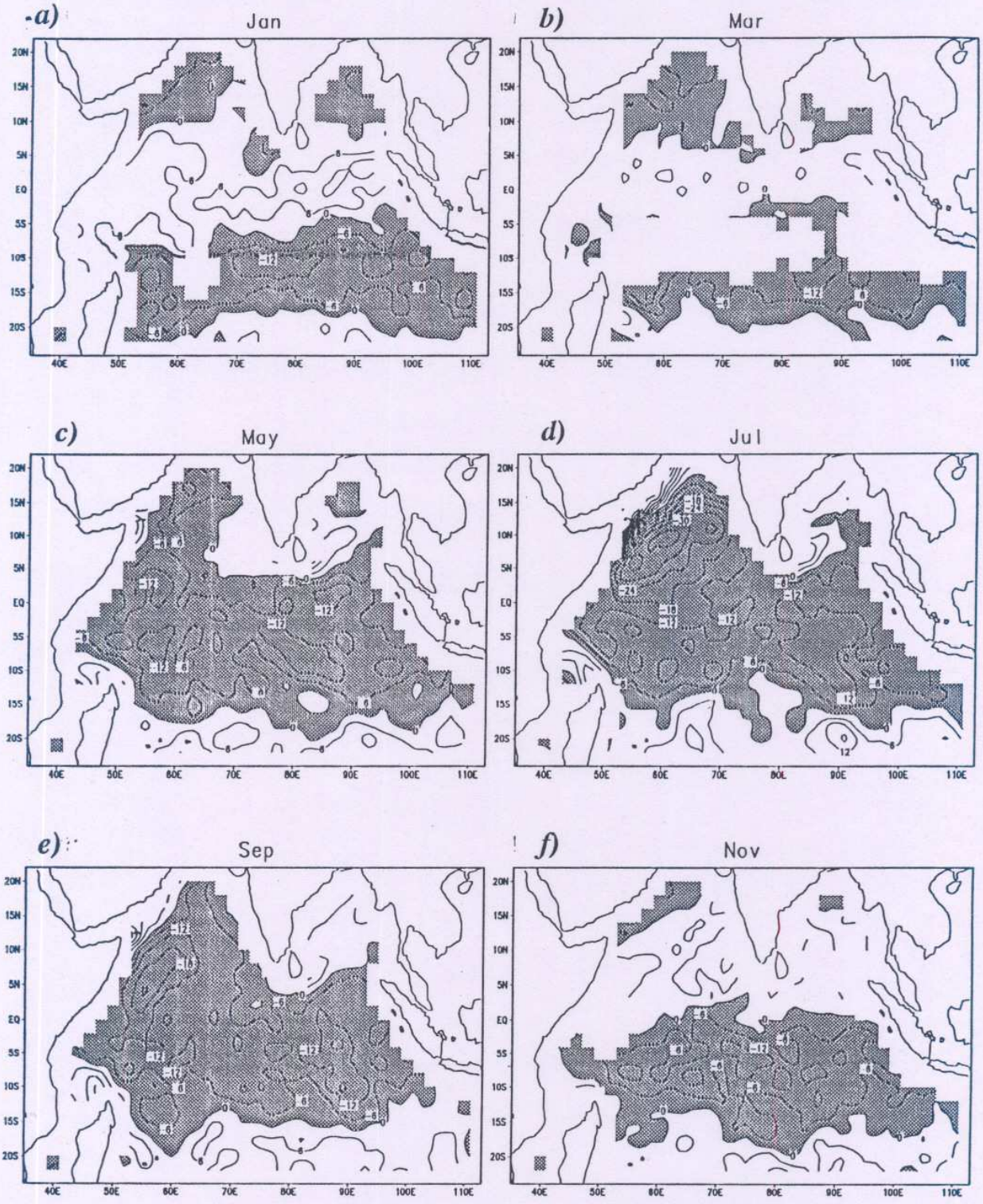

Fig. 5 : Same as Fig. 4 but for wind stress curl. Contour interval is $6*10^{-8}$ Nm^{-3} . Negative contours are shaded.

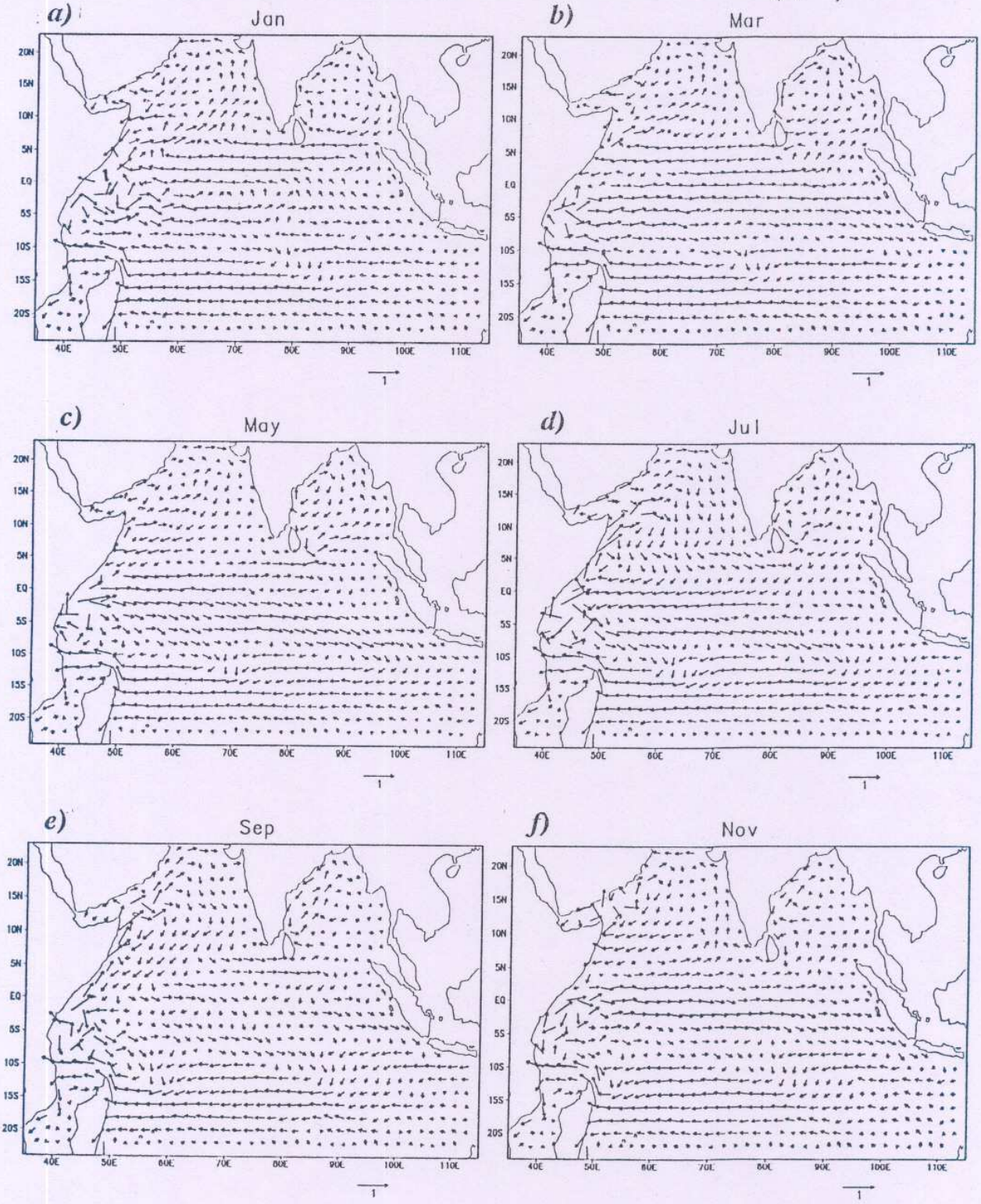

Fig. 6 : Model simulated upper layer currents in the tenth year of model simulation; (a) January, (b) March, (c) May, (d) July, (e) September and (f) November. The current arrows are of the vector field $\vec{V}'=\vec{V}/|\vec{V}|^{1/2}$ ($\vec{V}$ being the computed velocity vector).

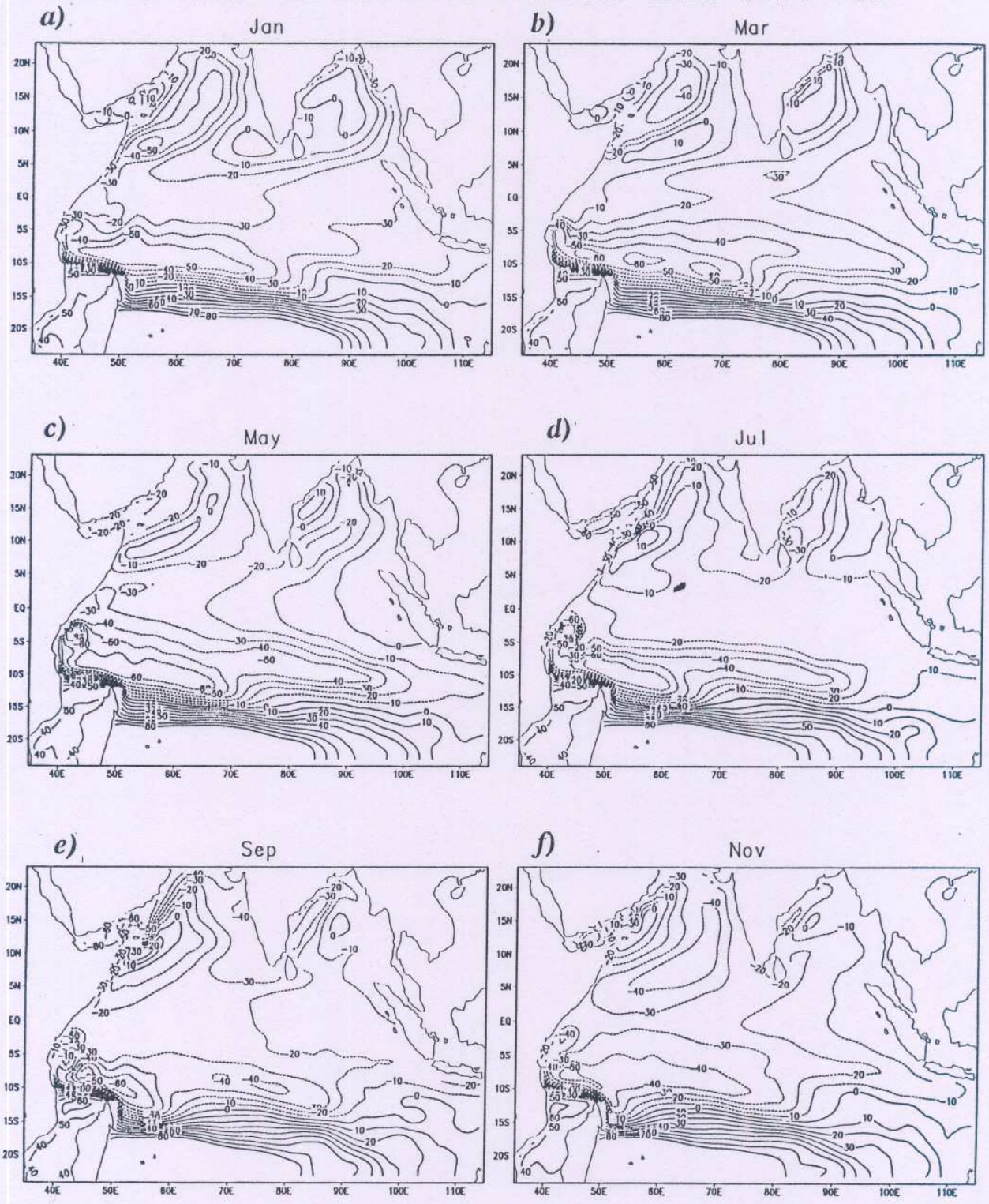

Fig. 7 : Same as fig. 6 but for model upper layer thickness deviation (ULTD) from the model initial depth. Contour interval is 10 m and dashed lines are negative contours.

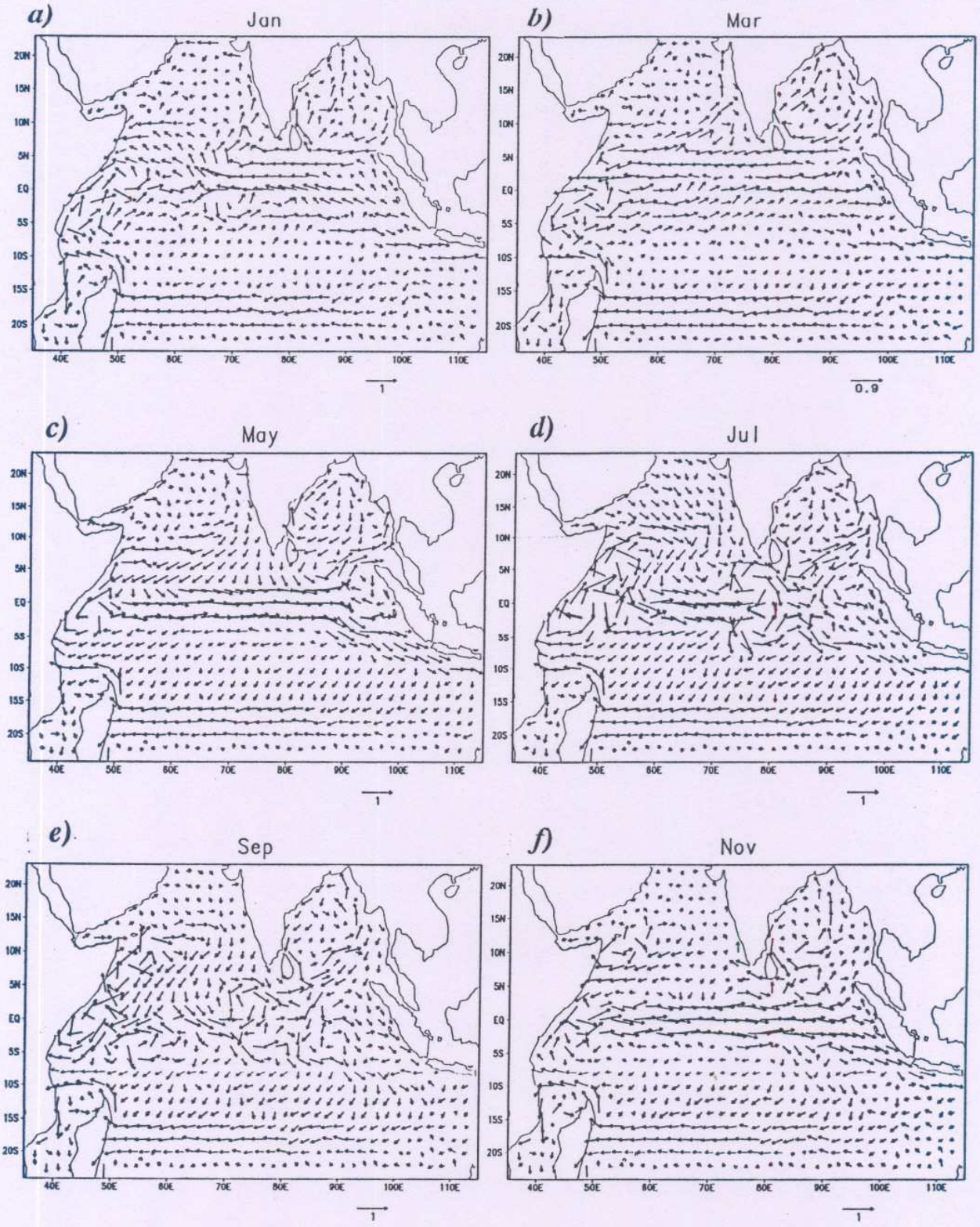

Fig. 8 : Same as fig. 6 but from the model simulation in case of 100 m initial depth case.

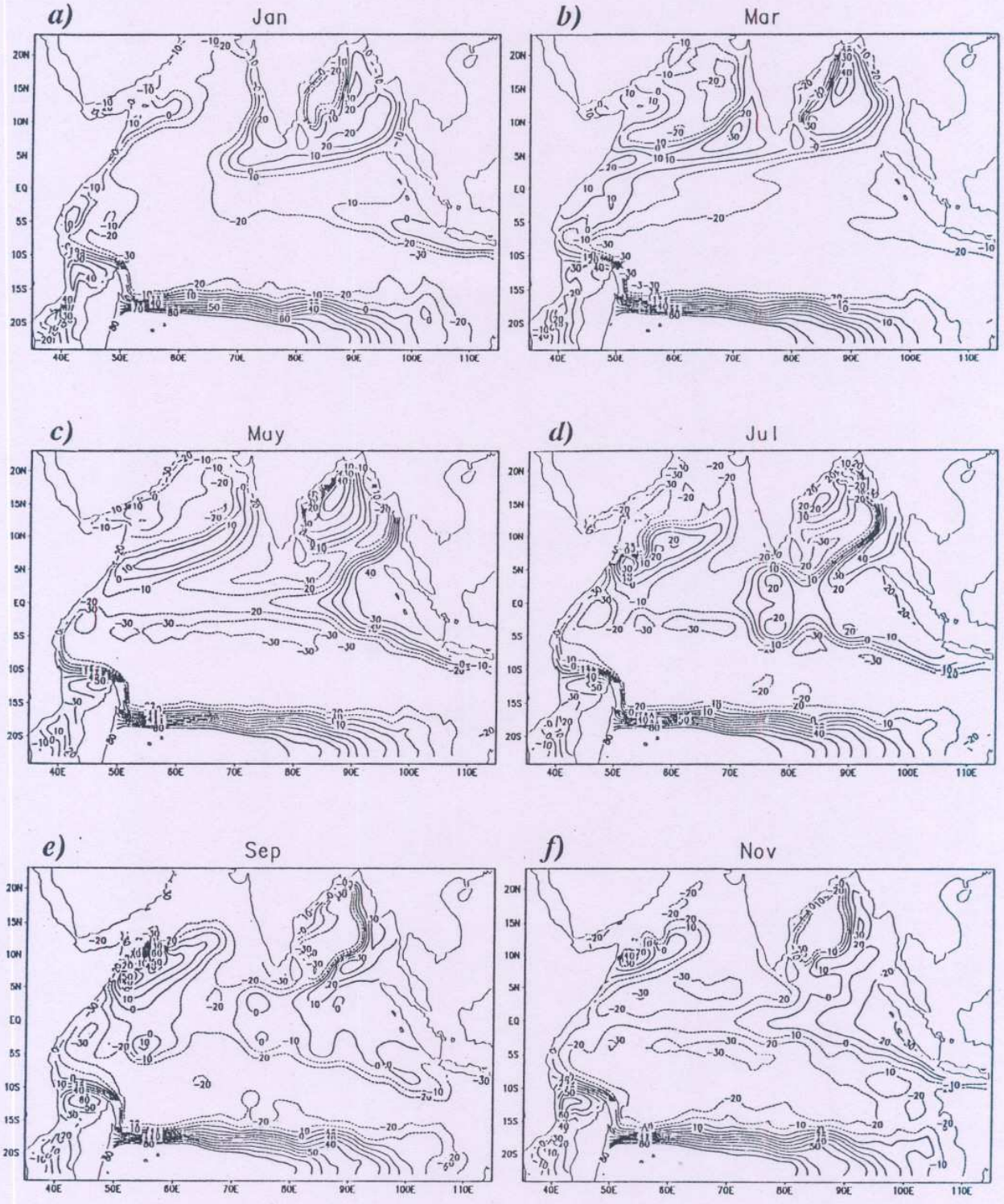

Fig. 9 : Same as fig. 7 but from the model simulation in case of 100 m initial depth case.

77–86 FSU WIND STRESS AND MODEL ULT STAND DEV

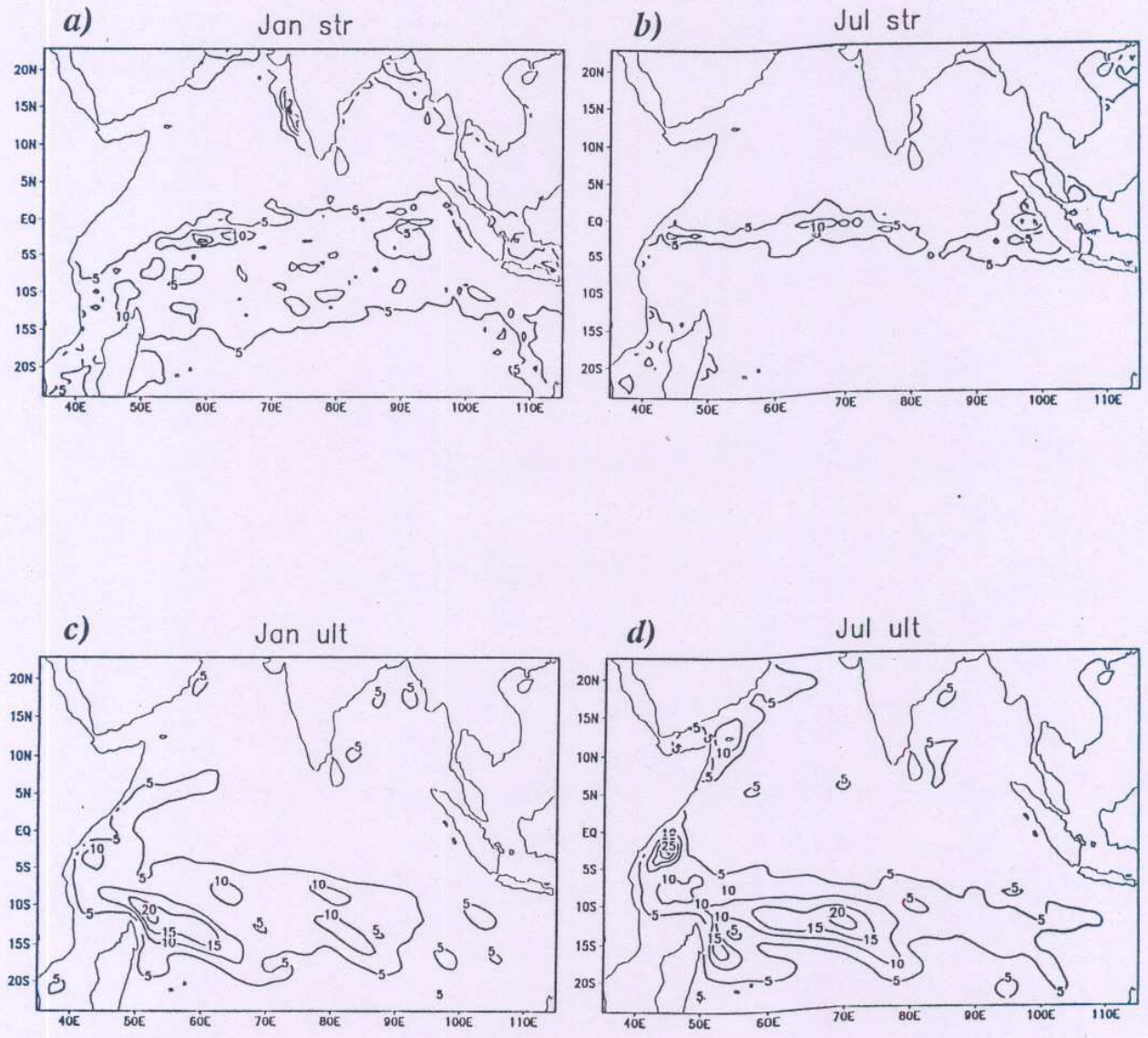

Fig.10 : The standard deviation of induced wind velocity magnitude shown in percentage departure from mean ; (a) January & (b) July. The contour interval is 5%. (c & d) same as (a) & (b) but for model ULTD. Contour interval is 5%.

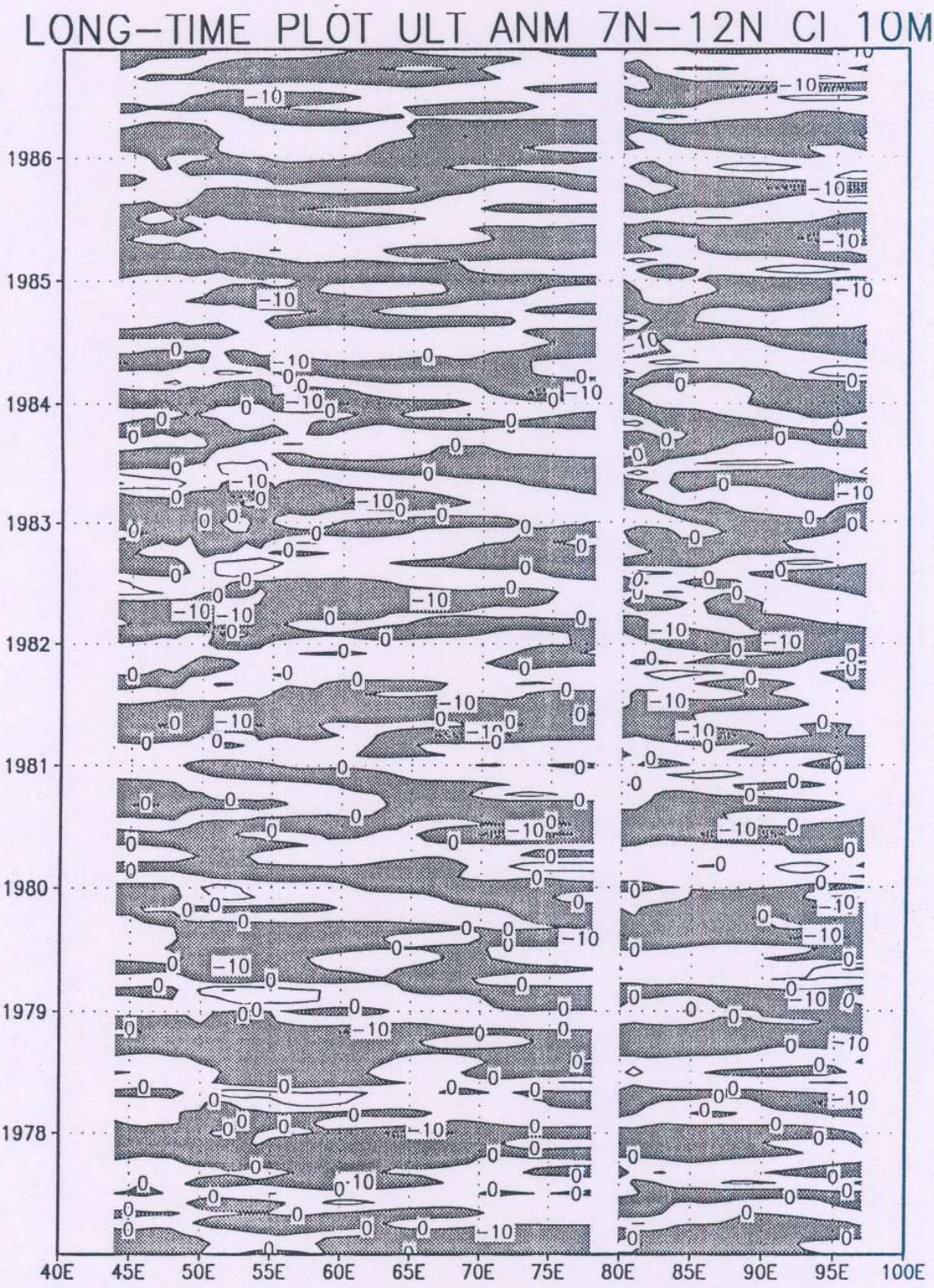

Fig.11 : Longitude-time cross section of ULT anomaly (taken from 10 year average value) averaged for the 5 degree latitudinal band between 7N and 12N. Negative Contours are shaded. Time axis starts with 16th January, 1977.

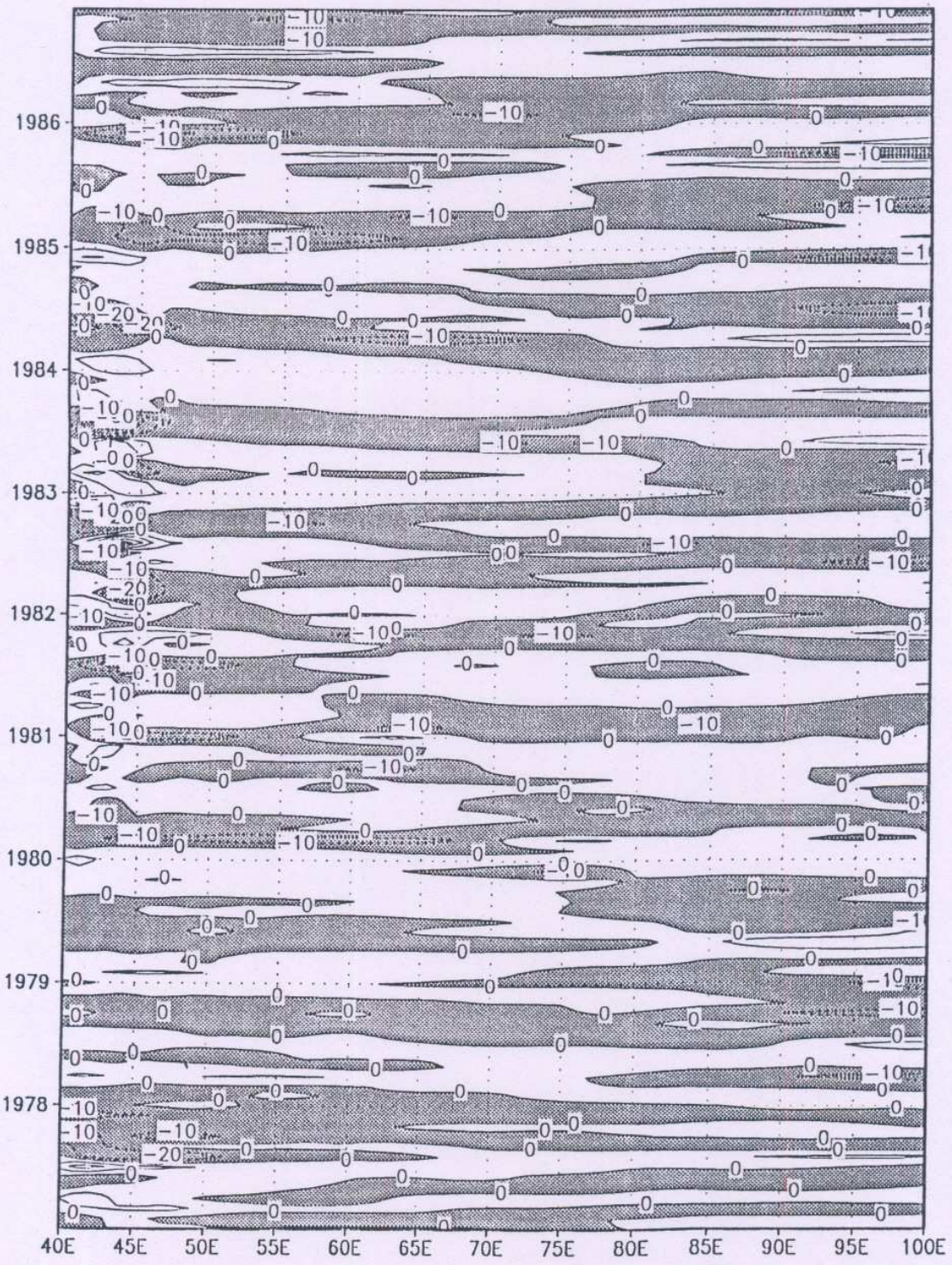

Fig.12 : Same as fig. 11 but for latitudinal band between 7S and 12S.

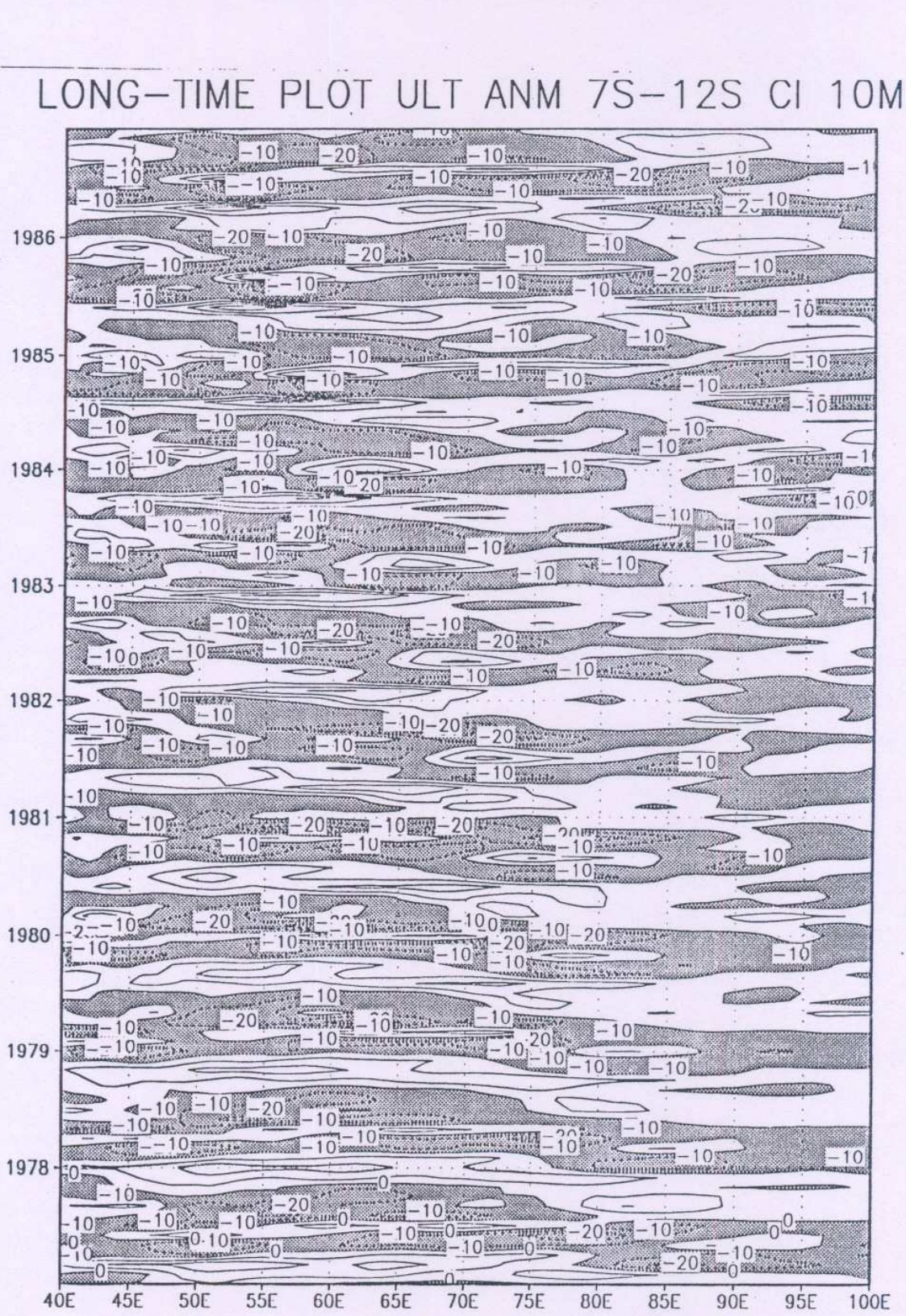

Fig.13 : Same as fig. 11 but for latitudinal band between 3N & 3S.

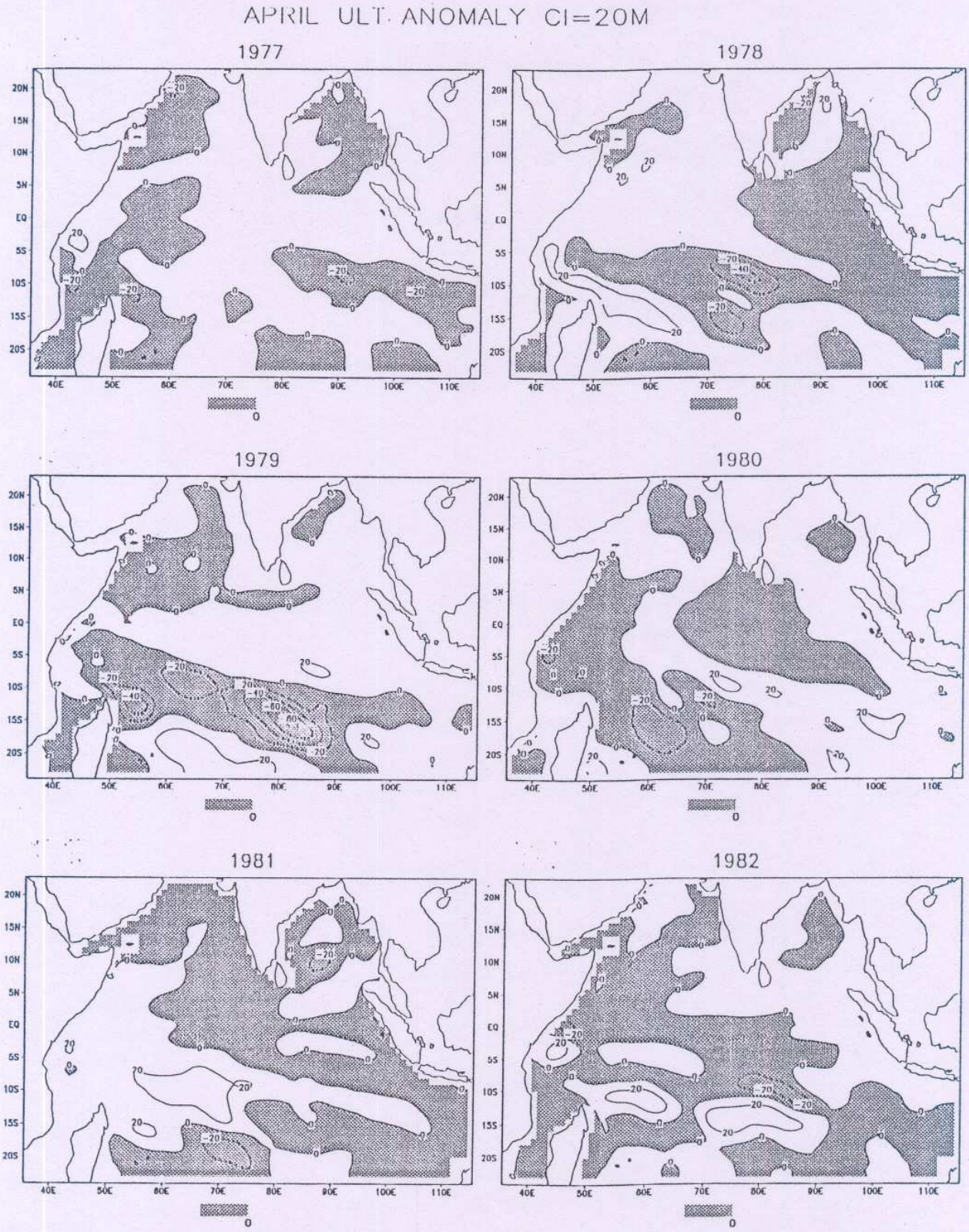

Fig.14 : The ten years model ULT anomaly (taken from ten year average value) for the month of April. Contour interval is 20 m and negative contours are shaded.

APRIL ULT ANOMALY CI=20M

1983

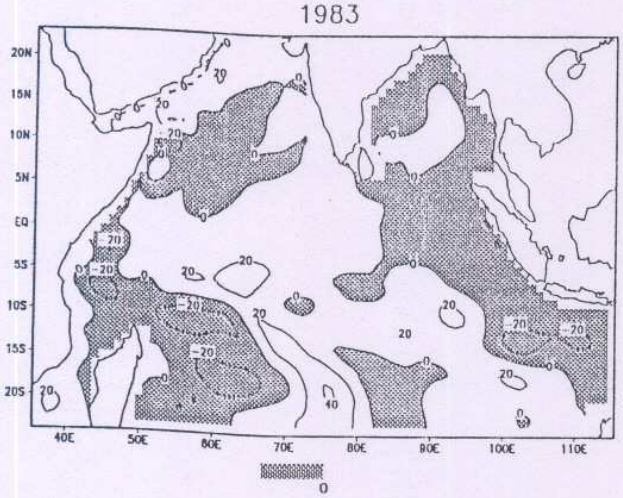

1984

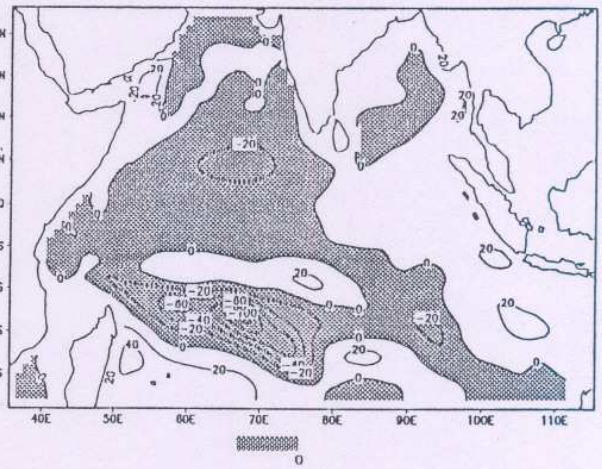

1985

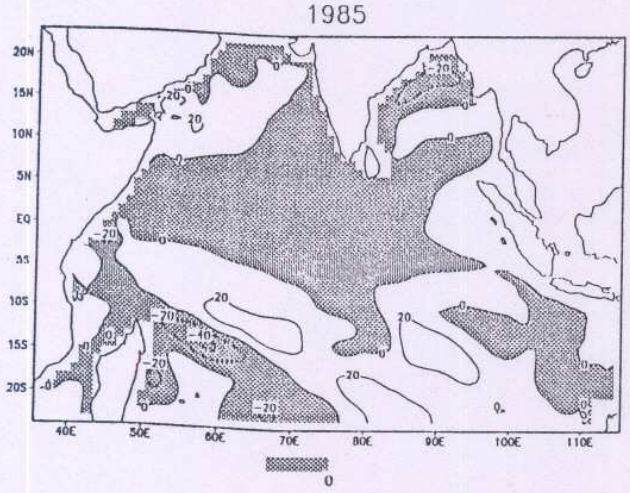

1986